Radboud Repository

Radboud University Nijmegen

PDF hosted at the Radboud Repository of the Radboud University Nijmegen

Multiwavelength campaign on Mrk 509

I. Variability and spectral energy distribution

J.S. Kaastra[1,2], P.-O. Petrucci[3], M. Cappi[4], N. Arav[5], E. Behar[6], S. Bianchi[7], J. Bloom[8], A.J. Blustin[9], G. Branduardi-Raymont[10], E. Costantini[1], M. Dadina[4], R.G. Detmers[1,2], J. Ebrero[1], P.G. Jonker[1,11,12], C. Klein[8], G.A. Kriss[13,14], P. Lubiński[15], J. Malzac[16,17], M. Mehdipour[10], S. Paltani[18], C. Pinto[1], G. Ponti[19], E.M. Ratti[1], R.A.N. Smith[10], K.C. Steenbrugge[20,21], and C.P. de Vries[1]

[1] SRON Netherlands Institute for Space Research, Sorbonnelaan 2, 3584 CA Utrecht, the Netherlands
[2] Sterrenkundig Instituut, Universiteit Utrecht, P.O. Box 80000, 3508 TA Utrecht, the Netherlands
[3] UJF-Grenoble 1 / CNRS-INSU, Institut de Planétologie et d'Astrophysique de Grenoble (IPAG) UMR 5274, Grenoble, F-38041, France
[4] INAF-IASF Bologna, Via Gobetti 101, 40129 Bologna, Italy
[5] Department of Physics, Virginia Tech, Blacksburg, VA 24061, USA
[6] Department of Physics, Technion-Israel Institute of Technology, Haifa 32000, Israel
[7] Dipartimento di Fisica, Università degli Studi Roma Tre, via della Vasca Navale 84, 00146 Roma, Italy
[8] Department of Astronomy, 601 Campbell Hall, University of California, Berkeley, CA 94720, USA
[9] Institute of Astronomy, University of Cambridge, Madingley Road, Cambridge CB3 0HA, UK
[10] Mullard Space Science Laboratory, University College London, Holmbury St. Mary, Dorking, Surrey, RH5 6NT, UK
[11] Harvard-Smithsonian Center for Astrophysics, 60 Garden Street, Cambridge, MA 02138, USA
[12] Department of Astrophysics, IMAPP, Radboud University Nijmegen, PO Box 9010, NL-6500 GL Nijmegen, the Netherlands
[13] Space Telescope Science Institute, 3700 San Martin Drive, Baltimore, MD 21218, USA
[14] Department of Physics and Astronomy, The Johns Hopkins University, Baltimore, MD 21218, USA
[15] Centrum Astronomiczne im. M. Kopernika, Rabiańska 8, PL-87-100 Toruń, Poland
[16] Université de Toulouse, UPS-OMP, IRAP, Toulouse, France
[17] CNRS, IRAP, 9 Av. colonel Roche, BP 44346, F-31028 Toulouse cedex 4, France
[18] ISDC Data Centre for Astrophysics, Astronomical Observatory of the University of Geneva, 16, ch. d'Ecogia, 1290 Versoix, Switzerland
[19] School of Physics and Astronomy, University of Southampton, Highfield, Southampton SO17 1BJ
[20] Instituto de Astronomía, Universidad Católica del Norte, Avenida Angamos 0610, Casilla 1280, Antofagasta, Chile
[21] Department of Physics, University of Oxford, Keble Road, Oxford OX1 3RH, UK

July 5, 2011

ABSTRACT

Context. Active galactic nuclei show a wealth of interesting physical processes, some of which are poorly understood. In a broader context, they play an important role in processes that are far beyond their immediate surroundings, owing to the high emitted power.

Aims. We want to address a number of open questions, including the location and physics of the outflow from AGN, the nature of the continuum emission, the geometry and physical state of the X-ray broad emission line region, the Fe-K line complex, the metal abundances of the nucleus and finally the interstellar medium of our own Galaxy as seen through the signatures it imprints on the X-ray and UV spectra of AGN.

Methods. We study one of the best targets for these aims, the Seyfert 1 galaxy Mrk 509 with a multiwavelength campaign using five satellites (XMM-Newton, INTEGRAL, Chandra, HST and Swift) and two ground-based facilities (WHT and PAIRITEL). Our observations cover more than five decades in frequency, from 2 μm to 200 keV. The combination of high-resolution spectroscopy and time variability allows us to disentangle and study the different components. Our campaign covers 100 days from September to December 2009, and is centred on a simultaneous set of deep XMM-Newton and INTEGRAL observations with regular time intervals, spanning seven weeks.

Results. We obtain a continuous light curve in the X-ray and UV band, showing a strong, up to 60% flux increase in the soft X-ray band during the three weeks in the middle of our deepest monitoring campaign, and which is correlated with an enhancement of the UV flux. This allows us to study the time evolution of the continuum and the outflow. By stacking the observations, we have also obtained one of the best X-ray and UV spectra of a Seyfert galaxy ever obtained. In this paper we also study the effects of the spectral energy distribution (SED) that we obtained on the photo-ionisation equilibrium. Thanks to our broad-band coverage, uncertainties on the SED do not strongly affect the determination of this equilibrium.

Conclusions. Here we present our very successful campaign and in a series of subsequent papers we will elaborate on different aspects of our study.

Key words. Galaxies: active – quasars: absorption lines – X-rays: general

1. Introduction

Active galactic nuclei (AGN) are compact sources with very high luminosities, located at the centres of galaxies. Accretion onto the super-massive black holes (SMBH) at their centres is generally believed to be the driving process for the activity. Thanks to their brightness, they form one of the richest laboratories for studying astrophysical processes. In this paper we present one of the deepest multiwavelength campaigns of an AGN, the Seyfert 1 galaxy Mrk 509. It is among the best for these studies because it is unique in combining X-ray brightness, outflow features, and significant but moderate variability. Below we introduce the most important astrophysical processes that are addressed by our study.

After our introduction of the relevant astrophysics, we briefly provide an overview in Sect. 3 of the target of our campaign, Mrk 509, followed by an overview of the observations in Sect. 4, and we present the spectral energy distribution (SED) and light curve in the subsequent sections. Details about various aspects of our study are deferred to subsequent papers of this series.

2. Astrophysics of AGN in the context of our campaign

2.1. Outflows from AGN

In recent years the potential importance of AGN outflows for the growth of super-massive black holes (Silk & Rees 1998; Blandford & Begelman 1999; King 2003; Blandford & Begelman 2004), the enrichment of the intergalactic medium (Furlanetto & Loeb 2001; Cavaliere et al. 2002), the evolution of the host galaxy (Scannapieco & Oh 2004), cluster cooling flows (Wu et al. 2000; Bower et al. 2001; Ciotti & Ostriker 2001; Borgani et al. 2002; Platania et al. 2002), the magnetisation of cluster and galactic gas (Daly & Loeb 1990; Furlanetto & Loeb 2001; Kronberg et al. 2001), and the luminosity function of AGN (Wyithe & Loeb 2003) has been widely recognised. However, for the lack of a better alternative, theoretical studies use the physical properties of the outflow (metallicity, mass, and kinetic energy flux) as free parameters because there are few observational constraints. To assess the importance of AGN outflows on the processes mentioned above, it is essential to establish the real mass flux, metallicity, and kinetic luminosity ($\dot{E}_k$) of AGN winds. Determining $\dot{E}_k$ requires answers to some fundamental questions. What is the physical state of the outflowing gas and what is its total column density? What is the distance of the gas from the central source?

The $\dot{E}_k$ of a shell-like, non-accelerating outflow is given by

$$\dot{E}_k \simeq \frac{1}{2} \Omega f_m R N_H m_p v^3, \tag{1}$$

where Ω is the solid angle occupied by the outflow, R the distance from the central source, N_H the total hydrogen column density, m_p the proton mass, $f_m = \rho/n_H m_p$ (1.43 for a plasma with proto-solar abundances) with ρ the mass density and n_H the hydrogen density, and v the outflow velocity. Spectral observations straightforwardly determine v, and Ω is expected to be $\sim \pi$ since 50% of all Seyfert 1s show outflow signatures (Crenshaw et al. 1999). Our campaign focuses on determining the two most uncertain quantities: N_H and R. Determining these is tightly connected to the physical state and location of the outflow, as explained below.

In the best studied AGN at least two to three ionisation components are needed to model the rich X-ray absorption spectrum.

In NGC 3783 there are three discrete components, which are most likely in pressure equilibrium, representing different phases of gas at the same distance from the nucleus (Krongold et al. 2003; Netzer et al. 2003). However, in NGC 5548 at least five ionisation components are needed if the X-ray absorber is modelled by a finite number of discrete absorption systems, and these absorbers cannot be in pressure equilibrium (Kaastra et al. 2002). Instead, a continuous, power-law distribution of N_H versus ionisation parameter ξ gives a better description of the data (Steenbrugge et al. 2003, 2005). In yet another case, Mrk 279, the distribution is continuous but more complicated than a simple power-law (Costantini et al. 2007).

Photo-ionisation modelling of the outflow yields the ionisation parameter $\xi \equiv L/nR^2$, where L is the 1–1000 Ryd ionising luminosity and n the hydrogen density. Independent measurements of n then determine R. The use of density sensitive X-ray lines is difficult and has not (yet) delivered robust results (Kaastra et al. 2004). Alternatively, when L changes, the outflow has to adjust to the new situation. How fast this happens depends on the recombination time scale, which scales as $\sim n^{-1}$. This method has been applied to a 280 ks XMM-Newton observation of NGC 3783 with wildly different results. From the RGS data $R > 10$ pc was inferred based on the lack of change in the deep O VII/O VIII absorption edges and the Fe-M UTA absorption complex (Behar et al. 2003). On the other hand, variability in the Fe XXV resonance line at 6.7 keV detected in the EPIC data (Reeves et al. 2004) implies $R < 0.2$ pc. From a 100 ks XMM-Newton observation of NGC 4051, $R \simeq 0.001$ pc was deduced for the highest ionisation gas (Krongold et al. 2007). However, the large amplitude variations (max / min = 12) and the short time scales (down to 100 s) make these results rather model-dependent; an analysis of Chandra LETGS data yielded distances in the range of 0.02–1 pc (Steenbrugge et al. 2009).

Density-sensitive lines have given more robust results in the UV, and in at least one case (NGC 3783) they yield a distance comparable to the one determined from densities based on recombination time scales. Using metastable transitions in [C III] $\lambda 1176$, Gabel et al. (2005) find a distance of ~25 pc for the absorbing gas in one of the components in NGC 3783. They find a comparable distance based on the recombination time for Si IV. Again using the [C III] metastable transitions, gas in one of the components in NGC 4151 lies at a distance of <0.1 pc (Kraemer et al. 2006). Using metastable levels in [Si II and [Fe II], Moe et al. (2009) find a distance for a low-ionisation outflow in the quasar SDSS J0838+2955 of ~ 3 kpc. Similarly, large distances for outflows have been found using similar density diagnostics in luminous quasars (Hamann et al. 2001; Dunn et al. 2010; Aoki et al. 2011; Arav et al. 2011).

In order to obtain a reliable density, we need both accurate ionic column densities, which yield the ionisation structure and total outflowing column density, and time variability on a suitable time scale, from which the location of the outflow can be constrained through monitoring. With the current generation of X-ray telescopes, only a handful of AGN with outflows have high enough fluxes to yield suitable data for such an ambitious programme. Of these targets, Mrk 509 is the most promising due to the following three attributes. 1) It is among the brightest X-ray AGNs in the sky. 2) It has an excellent X-ray line structure (Pounds et al. 2001; Smith et al. 2007; Detmers et al. 2010), not as deep and blended as NGC 3783, but not as shallow and sparse as Mrk 279. Mrk 509 is a representative example of a moderate outflow. 3) Mrk 509 varies on a time scale of a few days making it ideal for a spectral timing campaign. Other targets like MCG −6-30-15, Mrk 766, or NGC 4051 with long XMM-

Newton exposure times vary too rapidly to do this: within the characteristic time scales of 100–1000 s, it is simply not possible to get a high-quality grating spectrum.

2.2. Kinematics of the outflow as traced in the UV

Our campaign on Mrk 509 includes HST high-resolution ultraviolet spectral observations that are simultaneously with Chandra's grating X-ray observations. The ultraviolet spectra provide a more detailed view of the kinematics of the outflowing gas. Prior high-resolution spectral observations with the Far Ultraviolet Spectroscopic Explorer (FUSE) (Kriss et al. 2000) and the Space Telescope Imaging Spectrograph (STIS) on the Hubble Space Telescope (HST) (Kraemer et al. 2003) provide a good baseline for our observations, but these were both obtained nearly a decade before to our current campaign. The new UV spectra obtained with the Cosmic Origins Spectrograph (COS) on HST provide an updated view of the outflow, and enable us to examine long-term characteristics of the variability.

Although the UV absorbers are not necessarily a perfect tracer of the X-ray absorbing gas (Kriss et al. 2000; Kraemer et al. 2003), they provide insight into both lower ionisation absorbing components and portions of the high-ionisation outflow. Our COS observations yield accurate measurements of (or limits on) the column densities of C II, C IV, N V, O I, Si II – Si IV, S II, S III, Fe II, Fe III, and H I Lyα. Our limits or detections on the low-ionisation ions of Fe, Si, and S nicely complement the high-ionisation range covered by the RGS and the LETGS. Velocity-resolved measurements of the Li-like doublets of C IV and N V can be used to determine column densities and covering fractions of the outflowing gas (e.g., Arav et al. 2007).

2.3. Abundances in AGN

Studying the abundances, especially those of C, N, O, and Fe, of the gas in galaxies informs us about the ongoing enrichment processes through AGB star winds and supernova type Ia and II explosions. Therefore there has long been an interest in studying abundances with redshift to determine the star formation rate through history. Obvious sources for the study of the abundances are AGN, by taking advantage of their luminosity. Generally, the abundances in AGN have been determined from broad emission lines, however several assumptions make this method subject to systematic errors. Thanks to the improvement in atomic data, especially in the dielectronic recombination rates for iron, the excellent statistics in the combined RGS spectrum, and the simultaneous optical and hard X-ray fluxes to constrain the spectral energy distribution (SED), we can determine reliable and accurate relative abundances from the narrow absorption lines of the outflow observed in Mrk 509.

Since absolute abundances (i.e., metal abundances relative to hydrogen) cannot be measured directly from X-ray spectra, our UV observations of the Lyα line provide a constraint on the total hydrogen column density. The first absolute abundance estimate for an outflow was derived by our group from the UV spectra of Mrk 279, where absorption lines of H, C, N, and O were carefully modelled (Arav et al. 2007) to find abundances relative to solar for carbon (2.2±0.7), nitrogen, (3.5±1.1) and oxygen (1.6±0.8), which fully agree with the relative abundances of C, N, and O derived from the simultaneous X-ray spectra (Costantini et al. 2007). The apparently enhanced N/H and N/O ratios in the Mrk 279 outflow may hint at strong contributions from stellar winds from massive stars and AGB stars.

2.4. Broad emission lines

Broad lines, especially at the energy of the O VII triplet and the O VIII Lyα line, have been recently detected in high-resolution X-ray spectra (Kaastra et al. 2002; Ogle et al. 2004; Steenbrugge et al. 2005; Costantini et al. 2007; Longinotti et al. 2010). The width of the lines (about 1 Å, 10 000 km s^{-1}) is comparable to the width of the broad lines detected in the UV band and known to be produced in the so-called broad line region. In at least one case, the soft X-ray emission lines could be related, via a physical model (the locally optimally emitting clouds model, Baldwin et al. 1995), to the UV lines (Costantini et al. 2007). The contribution of the broad line region gas to the iron Kα line at 6.4 keV is not completely understood. For classical Seyfert 1 galaxies this contribution seems modest (e.g. <20% in Mrk 279, Costantini et al. 2010), while it may account for most of the line emission in specific objects (e.g. NGC 7213, Bianchi et al. 2008). The quality of the data of Mrk 509 allows us to significantly detect broad emission features around the O VII resonant line, the O VIII, N VII Lyα lines and the Ne IX triplet. The simultaneous observation of HST/COS and Chandra/LETGS allow us to connect the broad lines detected in the UV with the soft energy lines and even the iron Kα line.

2.5. Iron K complex

Mrk 509 also shows a rich variety of emission and absorption components in the Fe-K band. In particular, EPIC data from previous XMM-Newton observations shows evidence of a complex Fe-K emission line, with a narrow and neutral component possibly produced far from the source, plus a broad, ionised, and variable component possibly originating in the accretion disk (Pounds et al. 2001; Page et al. 2003; Ponti et al. 2009).

In addition, strong absorption features were found in the same data set at rest-frame energies 8–8.5 keV and 9.7 keV. These were interpreted as being produced by H-like iron K and K-shell absorptions associated with an outflow with mildly relativistic velocity of $0.14 - 0.2c$. The lines were found to be variable in energy and marginal in intensity, implying that variations in either the column density, geometry, and/or ionisation structure of the outflow were maybe common in this source (Dadina et al. 2005; Cappi et al. 2009).

The above properties, combined with the source brightness ($F_{2-10\,keV} \sim 2 - 5 \times 10^{-14}$ W m^{-2}) make Mrk 509 unique in attempting time-resolved spectral studies in the Fe-K band to follow the time evolution of both emission and absorption Fe-K features, and in disentangling the different physical components present in this source.

2.6. Continuum emission of Seyfert galaxies

The physical process at the origin of the X-ray emission of Seyfert galaxies is generally believed to be thermal Comptonisation. In this process, the soft UV photons coming from the accretion disk are up-scattered into the X-ray domain by the hot thermal electrons of the corona. A thermal distribution is generally preferred to a non-thermal one since the discovery, more than 15 years ago, of a high-energy cut-off near 100 keV in NGC 4151 by OSSE and Sigma (Jourdain et al. 1992; Maisack et al. 1993). Such a cut-off was not expected by the non-thermal models developed at that time to explain the power-law-like X-ray spectrum (e.g. Zdziarski et al. 1990). The presence of a high-energy cut-off has now been observed in a large

number of objects (Perola et al. 2002; Beckmann et al. 2005; Dadina 2008).

The cold (disk) and hot (corona) phases are expected to be radiatively linked: part of the cold emission, which gives birth to the UV bump, is produced by the reprocessing of part of the hot emission. Inversely the hot emission, at the origin of the broad-band X-ray continuum, is believed to be produced by Compton up-scattering of the soft photons, emitted by the cold phase, on the coronal energetic electrons. The system must then satisfy equilibrium energy balance equations, which depend on geometry and on the ratio of direct heating of the disk to that of the corona (Haardt & Maraschi 1991). In the limiting case of a 'passive' disk, the amplification of the Comptonisation process is only fixed by geometry. Therefore, if the corona is in energy balance, its temperature T_e and optical depth τ must satisfy a relation that can be computed for different geometries of the disk + corona configuration (e.g., Svensson 1996).

Realistic thermal Comptonisation spectra have been computed for more than two decades, and important effects like the anisotropy of the soft photon field have been precisely taken into account (Haardt 1993; Stern et al. 1995; Poutanen & Svensson 1996). These effects appear far from negligible. Noticeably, the spectral shape is significantly different for different disk-corona geometries but also for different viewing angles. Moreover, these effects underline the differences between realistic thermal Comptonisation spectra and the cut-off power-law approximation generally used to mimic them (Petrucci et al. 2001). This may have important consequences in the study of superimposed spectral components like the soft X-ray excess and/or the the iron line and the reflection hump, which require a precise determination of the underlying continuum.

A well known characteristic of thermal Comptonisation spectra, however, is that they are strongly degenerate, i.e., significantly different combinations of temperature and optical depth of the corona give the same power law slope in the 2–10 keV band. To break this degeneracy requires broad-band observations from UV to hard X-rays, the X-ray/γ-ray shape constraining the high-energy cut-off, which is directly linked to the corona temperature. The ratio of the UV to soft X-ray flux constrains the optical depth better. Stronger and less ambiguous constraints on the nature of the coronal plasma can also be obtained from multiwavelength (from UV to hard X-rays/γ-rays) variability studies, as they provide direct insight into the way the emitting particles are heated and cooled. Indeed, variations in the X-ray spectral shape may be produced by intrinsic changes in the hot corona properties (e.g. changes of the heating process efficiency) and/or by variations in the external environment, such as changes in the soft photon flux (and consequently in the coronal cooling) produced by the cold phase (Malzac & Jourdain 2000; Petrucci et al. 2000). For example, thermal Comptonisation models, where hot and cold phases are in radiative equilibrium, predict that the X-ray spectrum of the sources should harden when the energy of the high-energy cut-off increases (e.g. Haardt et al. 1997). Indeed a correlation between Γ and T_e has been observed in different objects (Petrucci et al. 2000; Zdziarski & Grandi 2001), thus giving strong support to a thermal nature of the corona particle distribution. The analysis of the one month, simultaneous IUE/RXTE monitoring campaign on NGC 7469, performed in 1996, is also in agreement with thermal Comptonisation emission (Nandra et al. 2000; Petrucci et al. 2004).

The XMM-Newton/INTEGRAL monitoring of Mrk 509 presented here provides an ideal data set to test Comptonisation models and to derive further constraints on the physical pa-

rameters and geometry of the source, as well as on the precise shape of spectral components such as the soft-X-ray excess, the outflow, and the reflection component. It should also be noted that a good knowledge of the SED up to 100 keV is very important input for the photo-ionisation modelling of the absorption/emission features produced by these outflows.

3. Mrk 509

Mrk 509 was detected as a Seyfert 1 galaxy with a photographic magnitude $m_{pg} = 13$ and a size of $10''$ (Markarian & Lipovetskij 1973). It has a redshift of 0.034397 (Huchra et al. 1993) and broad (FWHM $4\,500$ km s^{-1}) and narrow optical emission lines (Markarian 1973). Its optical luminosity is high for a Seyfert 1 galaxy, and it puts Mrk 509 close to the limit between Seyfert galaxies and QSOs (Kopylov et al. 1974).

The host galaxy extends approximately east-west (Magnitskaia & Saakian 1976) and has an axial ratio $b/a \sim 0.85$ (Dahari & De Robertis 1988; Kirhakos & Steiner 1990). Mrk 509 presently shows no nearby neighbours (Magnitskaia & Saakian 1976), the closest spiral galaxy is at a projected distance of 0.3 Mpc (Fuentes-Williams & Stocke 1988), but the asymmetric halo to the south (MacKenty 1990) is direct evidence for strong interactions at some point in the recent past.

In almost any wavelength band that opened its window, Mrk 509 has been one of the first AGN to be studied, thanks to its brightness, and several well-known astrophysicists today have investigated this object in earlier stages of their careers.

In the radio band, Mrk 509 was discovered at 3.9 cm in 1976 (Mingaliev et al. 1978). Spatially resolved measurements at 6 and 20 cm show an asymmetric structure of $1.4''\times0.5''$ in PA 124° (Ulvestad & Wilson 1984; Unger et al. 1987), corresponding to a linear size of about 1 kpc. This core is surrounded by more diffuse emission, visible at 20 cm, with a size comparable to the optical size ($10 \times 8''$, or 7×5 kpc (Singh & Westergaard 1992). The radio emission seems to be preferentially aligned at PA $-40°$ to $-60°$, coinciding with the preferred direction of the optical polarisation (Singh & Westergaard 1992; Martin et al. 1983).

In the infrared the first observations date back to 1975 (Stein & Weedman 1976; Allen 1976). The spectrum in the 1–$10\,\mu$m band is approximately a power law (Rieke 1978; Glass et al. 1982; McAlary et al. 1983). Contrary to several other Seyferts, Mrk 509 shows no evidence of strong dust features in infrared spectra (Roche et al. 1984; Moorwood 1986). The variability in the mid-IR is much weaker than at shorter wavelengths, with a possible delay of two to three months (Glass 2004). This suggests that the bulk of the IR emission originates far from the nucleus.

Quantitative measurements of the optical broad and narrow emission lines were first presented by Osterbrock (1977) and de Bruyn & Sargent (1978). Since then, dozens of papers have appeared with refined measurements and models for the line profiles and intensity ratios. The size of the broad emission line region in the Hβ line has been estimated as 80 light days (0.07 pc) based on reverberation studies (Peterson et al. 1998).

Perhaps the most detailed study of interest for our project has been the mapping of the [O III] λ5007 line by Phillips et al. (1983). They show that the line has two components. There is a rotating, low-ionisation gas disk, coinciding with hot stellar components, which is photo-ionised by the UV radiation of young hot stars. The rotation axis has approximately the same direction as the radio emission and the preferred polarisation angle

of the optical emission mentioned before. The second component is expanding, high-ionisation gas, which is photo-ionised by the nucleus. The line profile of that component is consistent with outflowing gas up to velocities of -800 km s^{-1}. It extends out to about 5 kpc from the nucleus. Outflowing gas is seen at opposite sides of the nucleus, indicating that the outflow is approximately face-on. A similar spatial extent is seen in a few other narrow emission lines (Winge et al. 2000). Approximately the same region also shows broad Hβ line emission, most likely caused by scattered nuclear light in the narrow line region (Mediavilla et al. 1998). X-rays from the nucleus travel through these media, and the lowewst ionised X-ray absorbers may show the imprint of this material on the spectrum.

The first UV spectra were presented in 1980, with measurements of the Lyα line flux using the IUE satellite (Wu et al. 1980). Significantly better spectra were subsequently obtained with HST (Crenshaw et al. 1995, 1999; Kraemer et al. 2003) and FUSE (Kriss et al. 2000).

In X-rays, the first detection was made with Ariel V in 1974–1976 in the 2–10 keV band (Cooke et al. 1978). Soon the first (power-law) spectra were fitted (Mushotzky et al. 1980), and the source was detected at higher energies, beyond 40 keV (Dil et al. 1981) and up to about 200 keV (Pietsch et al. 1981; Rothschild et al. 1983). It was one of the first sources where a soft X-ray excess was discovered with HEAO1-A2 (Singh et al. 1985), the first iron line detection dated to 1987 with EXOSAT (Morini et al. 1987), and the reflection component was revealed by Ginga (Pounds et al. 1994).

Variability was discovered first in the optical band (Magnitskaia & Saakian 1976). They found variations of about a magnitude on a time scale of several months, but a comparison with observations 21 years before showed a similar flux level. This is one of the desired properties for the purpose of our campaign: significant variability on suitable time scales, with a limited range of flux levels. Since then, variability has been found in all energy bands from radio (Mingaliev et al. 1978), infrared continuum (Glass 2004), optical polarisation (Martin et al. 1983), broad emission lines (Peterson et al. 1982, 1984; Rosenblatt et al. 1992), UV (Chapman et al. 1985), and X-rays (Dower et al. 1980).

There have been many papers that derive the mass of the central SMBH using a variety of methods. Derived numbers range from 1.4×10^9 M$_\odot$ in one of the oldest determinations, based on the correlation of the Hβ intensity with the full-width at zero intensity (Liu 1983) to $1.43 \pm 0.12 \times 10^8$ M$_\odot$ for a modern estimate based on reverberation mapping of optical broad lines (Peterson et al. 2004).

4. Observations

We have obtained data from seven different observatories during our campaign. At the core of our programme are ten observations of approximately 60 ks each, with XMM-Newton, spaced by four days. We used the data of all instruments on XMM-Newton: Reflection Grating Spectrometer (RGS), EPIC (pn and MOS), and Optical Monitor (OM). For this last instrument, all filters except for the white light filter were used, and we also obtained a spectrum with the optical grism for each observation. Observations with the UV grism were not allowed for operational reasons.

Simultaneously with our ten XMM-Newton observations, we obtained data with INTEGRAL to observe the hard X-rays. Three weeks after the end of the XMM-Newton monitoring, we did simultaneous observations with Chandra
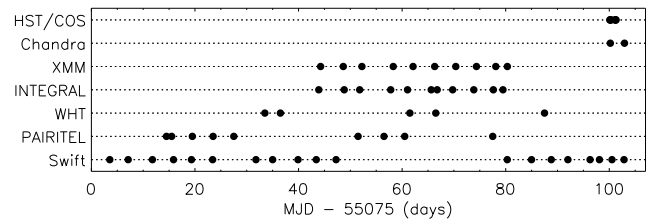

Fig. 1. Timeline of our monitoring campaign of Mrk 509. The first observation, with Swift, started on September 4, 2009, and the last observation, with Chandra, ended on December 13, 2009.

(Low Energy Transmission Grating (LETGS) with the HRC-S camera), together with the Hubble Space Telescope (HST) Cosmic Origins Spectrograph (COS). Due to operational constraints, these observations could not coincide with the XMM-Newton/INTEGRAL monitoring.

Before our XMM-Newton/INTEGRAL observations, and in between the XMM-Newton and Chandra/HST observations, we monitored Mrk 509 with Swift, using both its X-ray telescope (XRT) and the UltraViolet and Optical Telescope (UVOT). This was in order to obtain a continuous monitoring and to allow us to study the flux before the start of our campaign. This is important because absorption components may respond with a delay to continuum variations.

Finally, throughout our high-energy campaign, we obtained optical spectroscopy and photometry. We have five observations with the 4.2 m William Herschel Telescope (WHT) at La Palma, photometry with the ACAM camera using the Sloan g, r, i and Z filters, and low-resolution spectroscopy with the VPH disperser. Furthermore, we obtained nine observations with the 1.3 m PAIRITEL (Peters Automated IR Imaging Telescope), with photometry in the J, H, and K bands. Table 1 gives some details on our observations, and in Fig. 1 we show a graphical overview of the timeline of our campaign.

5. Light curve

The light curves in the X-ray band (0.3–1.0 keV, 2–10 keV and 20–60 keV) and in UV (2310 Å) are shown in Fig. 2. More details and the interpretation of these light curves are given in subsequent papers of our series (e.g. Mehdipour et al. 2011; Petrucci et al. 2011). The flux was at a typical flux level, compared with archival observations. Right in the middle of our observing campaign, the source showed a significant brightening by $\sim 50\%$, in particular in the soft X-ray band, and with a smaller amplitude in the UV and hard X-ray bands. This allowed us to study the response of the absorption components to this brightening, and thanks to our broad-band measurements we can constrain the emission mechanisms for the continuum components.

6. Spectral energy distribution

The broad-band spectral energy distribution (SED) is essential for obtaining the ionisation balance needed for the photo-ionisation modelling of the outflow. The multiwavelength nature of our campaign gave us almost simultaneous coverage of the total spectrum, which allowed us to constrain the exact shape of the SED to high accuracy.

We need two different SEDs for our campaign. The first describes the average SED during the *XMM-Newton* part of the

Table 1. The observation log of our Mrk 509 campaign.

Telescope	Obs.	ID	Start time (UTC) yyyy-mm-dd@hh:mm	Span (ks)	Telescope	Obs.	ID	Start time (UTC) yyyy-mm-dd@hh:mm	Span (ks)
Chandra	1	11387	2009-12-10@04:54	131.4	HST/COS	1	lbdh01010	2009-12-10@02:48	2.0
Chandra	2	11388	2009-12-12@22:33	48.6	HST/COS	2	lbdh01020	2009-12-10@04:07	2.7
XMM-Newton	1	0601390201	2009-10-15@06:19	57.1	HST/COS	3	lbdh01030	2009-12-10@05:42	5.5
XMM-Newton	2	0601390301	2009-10-19@15:20	59.9	HST/COS	4	lbdh01040	2009-12-10@08:54	2.7
XMM-Newton	3	0601390401	2009-10-23@05:41	60.5	HST/COS	5	lbdh02010	2009-12-11@02:46	2.0
XMM-Newton	4	0601390501	2009-10-29@06:55	60.5	HST/COS	6	lbdh02020	2009-12-11@04:05	2.7
XMM-Newton	5	0601390601	2009-11-02@02:46	62.4	HST/COS	7	lbdh02030	2009-12-11@05:41	2.7
XMM-Newton	6	0601390701	2009-11-06@07:00	62.7	HST/COS	8	lbdh02040	2009-12-11@07:16	5.5
XMM-Newton	7	0601390801	2009-11-10@08:42	60.5	WHT	1	1372032–154	2009-10-04@22:50	1.6
XMM-Newton	8	0601390901	2009-11-14@08:27	60.5	WHT	2	1372732–166	2009-10-07@20:10	3.6
XMM-Newton	9	0601391001	2009-11-18@02:08	65.1	WHT	3	1378102–127	2009-11-01@20:55	2.4
XMM-Newton	10	0601391101	2009-11-20@07:40	62.4	WHT	4	1378849–900	2009-11-06@19:30	5.4
INTEGRAL	1	07200160001	2009-10-14@21:55	127.7	WHT	5	1382682–702	2009-11-27@19:42	1.5
INTEGRAL	2	07200160002	2009-10-19@19:38	120.1	Swift	1	00035469005	2009-09-04@13:18	0.9
INTEGRAL	3	07200160003	2009-10-22@19:29	124.3	Swift	2	00035469006	2009-09-08@02:30	1.5
INTEGRAL	4	07200160004	2009-10-28@19:08	110.7	Swift	3	00035469007	2009-09-12@18:52	0.5
INTEGRAL	5	07200160005	2009-11-01@01:07	122.3	Swift	4	00035469008	2009-09-16@20:36	1.1
INTEGRAL	6	07200160006	2009-11-05@15:00	63.0	Swift	5	00035469009	2009-09-20@07:51	1.1
INTEGRAL	7	07200160011	2009-11-06@18:32	59.0	Swift	6	00035469010	2009-09-24@09:51	1.3
INTEGRAL	8	07200160007	2009-11-09@18:18	120.7	Swift	7	00035469011	2009-10-02@18:45	1.0
INTEGRAL	9	07200160008	2009-11-13@20:13	122.3	Swift	8	00035469012	2009-10-05@23:59	1.0
INTEGRAL	10	07200160009	2009-11-17@14:48	61.2	Swift	9	00035469013	2009-10-10@21:37	1.1
INTEGRAL	11	07200160010	2009-11-19@11:23	110.7	Swift	10	00035469014	2009-10-14@10:09	1.4
PAIRITEL	1	166.2	2009-09-15@04:45	0.8	Swift	11	00035469015	2009-10-18@05:56	1.0
PAIRITEL	2	166.2	2009-09-16@04:35	0.8	Swift	12	00035469016	2009-11-20@07:18	1.0
PAIRITEL	3	166.3	2009-09-20@04:51	0.8	Swift	13	00035469017	2009-11-24@23:39	1.0
PAIRITEL	4	166.4	2009-09-24@03:55	0.8	Swift	14	00035469018	2009-11-28@19:13	1.2
PAIRITEL	5	166.5	2009-09-28@03:24	0.8	Swift	15	00035469019	2009-12-02@00:18	1.3
PAIRITEL	6	166.7	2009-10-22@02:55	0.8	Swift	16	00035469020	2009-12-06@07:07	1.2
PAIRITEL	7	166.8	2009-10-27@04:06	0.8	Swift	17	00035469021	2009-12-08@02:30	1.1
PAIRITEL	8	166.9	2009-10-31@03:21	0.8	Swift	18	00035469022	2009-12-10@12:36	1.2
PAIRITEL	9	166.10	2009-11-17@03:19	0.8	Swift	19	00035469023	2009-12-12@20:30	1.0

campaign, which is needed for the analysis of the stacked RGS spectrum. The second one is needed for the Chandra LETGS and HST COS part of the campaign, when the source had a lower flux level. Table 2 shows the flux points of every instrument used to create the SED shown in Fig. 3. The statistical uncertainties on the flux are much lower than the reported values (except in the case of INTEGRAL), therefore we list the systematic uncertainties due to calibration uncertainties.

6.1. X-ray SED

We used the best fit RGS model (model 2 of Detmers et al. 2011) for the spectrum between 7–38 Å. We correct for both the intrinsic absorption (the ionised outflow) and the Galactic ISM absorption. For the flux between 1.2 Å (10 keV) and 7 Å (1.77 keV), we used the EPIC-pn data. Above 10 keV we used the INTEGRAL data, which were obtained simultaneous with the XMM-Newton observations. This gives us the continuum flux up to ~ 200 keV. Beyond that, the SED is extrapolated using the model described in Petrucci et al. (2011).

We compared the Chandra LETGS flux in two different energy bands with the non-contemporaneous RGS flux to obtain the flux variations in the soft (20 − 35 Å) and hard (7 − 10 Å) X-ray bands. The RGS flux in these bands is 66% and 30% higher than the LETGS flux, respectively. The soft X-ray flux for the RGS observation for $\lambda > 37$ Å is obtained by scaling the LETGS continuum by a factor of 1.66. As we have no information on the X-ray flux above 10 keV during the LETGS observation, and the uncertainty on the LETGS spectrum for $\lambda < 7$ Å increases, we estimate the flux for the Chandra observation for $\lambda < 7$ Å by dividing our model for XMM-Newton/INTEGRAL by a factor of 1.30.

6.2. EUV extrapolation

The EUV spectrum produces most of the ionising flux; however, it is also the most uncertain part of the SED, as there are no data between 50 and 912 Å. LETGS formally measures up to 175 Å, but due to the Galactic absorption, the flux is low and also the modelling of the higher spectral orders becomes more uncertain at longer wavelengths. We therefore have to interpolate our SED between the soft X-rays and the UV. There are several options for doing this. Our baseline model is a power-law interpolation between 50–943 Å (the last FUSE data point). For the XMM-
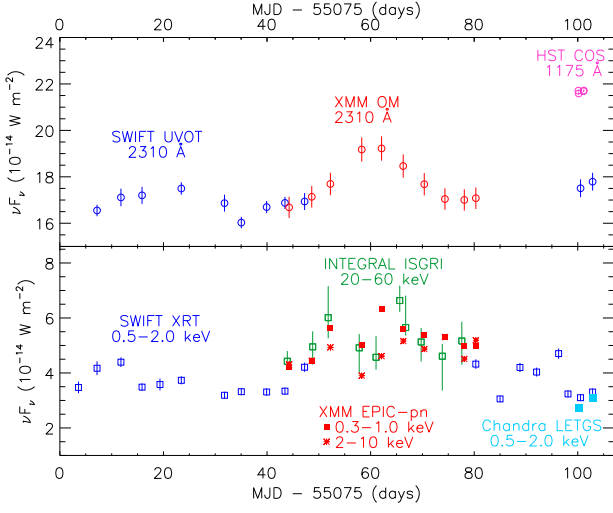
Fig. 2. Top panel: UV light curve of Mrk 509 as obtained with Swift/UVOT, XMM-Newton/OM, and HST/COS. The data have been corrected for extinction. Bottom panel: X-ray light curve as obtained by Swift/XRT, XMM-Newton/pn, Chandra/LETGS, and INTEGRAL/ISGRI. These data have also been corrected for Galactic absorption. For the pn data, the squares correspond to the 0.3–1.0 keV band, the stars to the 2–10 keV band. Note that 10^{12} JyHz equals 10^{-14} W m^{-2} (10^{-11} in c.g.s. units).
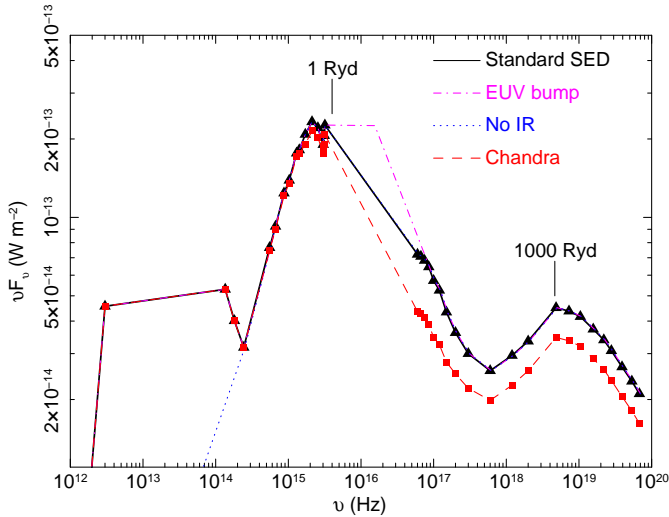

Fig. 3. The SED used of Mrk 509 for the time-averaged XMM-Newton and Chandra observations. Data points from Table 2 are indicated with triangles and squares.

Newton epoch this power law has a photon index of 2.39, for the Chandra epoch 2.53. Alternatively, we consider some kind of big blue bump, by extrapolating the RGS spectrum with a power law, using its slope near 30 Å (photon index 2.58) up to the point (193 Å) where it matches the extrapolation from the UV with a photon index of −2. The different extrapolations between the X-ray and UV data are shown in Fig. 3.

6.3. UV SED

The UV part of the SED was derived from archival FUSE data and from the HST COS data of our campaign. As FUSE and COS share a common wavelength band, the FUSE archival

Table 2. Continuum fluxes corrected for Galactic and intrinsic absorption during the XMM-Newton and Chandra parts of the campaign.

Frequency (Hz)	E/λ	νF_ν [a]	νF_ν [b]	Unc.[c] (%)	Instr.[d]
3.91×10^{19}	162 keV	2.67	2.05	50	INTEGRAL
2.79×10^{19}	115 keV	3.08	2.37	30	INTEGRAL
2.20×10^{19}	91 keV	3.39	2.60	10	INTEGRAL
1.57×10^{19}	65 keV	3.72	2.86	10	INTEGRAL
1.05×10^{19}	43 keV	4.16	3.20	10	INTEGRAL
7.30×10^{18}	30 keV	4.37	3.36	10	INTEGRAL
4.84×10^{18}	20 keV	4.50	3.46	10	INTEGRAL
2.00×10^{18}	1.5 Å	3.35	2.58	5	pn
1.20×10^{18}	2.5 Å	2.95	2.27	5	pn
6.00×10^{17}	5.0 Å	2.58	1.98	5	pn/RGS
3.00×10^{17}	10 Å	3.00	2.21	5	RGS
2.00×10^{17}	15 Å	3.61	2.51	5	RGS
1.50×10^{17}	20 Å	4.33	2.78	5	RGS
1.20×10^{17}	25 Å	5.25	3.24	5	RGS
1.00×10^{17}	30 Å	5.72	3.46	5	RGS
8.57×10^{16}	35 Å	6.46	3.89	5	RGS
7.50×10^{16}	40 Å	6.83	4.12	5	LETGS
6.67×10^{16}	45 Å	7.08	4.27	5	LETGS
6.00×10^{16}	50 Å	7.21	4.35	5	LETGS
3.18×10^{15}	943 Å	22.6	20.8	10	FUSE
3.13×10^{15}	960 Å	20.6	19.0	10	FUSE
3.05×10^{15}	984 Å	20.6	18.8	10	FUSE
3.02×10^{15}	993 Å	19.0	17.5	10	FUSE
2.55×10^{15}	1175 Å	22.1	20.3	5	FUSE
2.12×10^{15}	1415 Å	23.3	21.5	5	COS
1.71×10^{15}	1750 Å	20.8	19.1	5	COS
1.42×10^{15}	2120 Å	18.2	17.5	3	OM
1.30×10^{15}	2310 Å	17.6	17.1	3	OM
1.03×10^{15}	2910 Å	13.9	13.5	3	OM
8.72×10^{14}	3440 Å	12.4	12.1	3	OM
6.67×10^{14}	4500 Å	9.24	8.98	3	OM
5.52×10^{14}	5430 Å	7.65	7.46	4	OM
2.44×10^{14}	1.23 μm	3.17		10	J[e]
1.81×10^{14}	1.66 μm	4.01		10	H[e]
1.35×10^{14}	2.22 μm	5.30		10	K[e]
3.00×10^{12}	100 μm	4.56		15	IRAS[e]
3.00×10^{10}	1 cm	4.56×10^{-7}		15	Radio[e]

[a] For the time-averaged XMM-Newton spectrum, in units of 10^{-14} W m^{-2} (or 5.034 photons m^{-2} s^{-1} Å^{-1})

[b] For the time-averaged Chandra spectrum, in units of 10^{-14} W m^{-2} (or 5.034 photons m^{-2} s^{-1} Å^{-1})

[c] Estimated systematic and statistical uncertainty

[d] Instrument used to derive the flux

[e] Values obtained from the literature for the J, H, K, IRAS and radio bands; see text for references.

fluxes were scaled to the COS flux level, assuming that the spectral shape remained the same.

The full description of the COS data reduction can be found in Kriss et al. (2011). In short, the COS data were flat-field corrected and additional wavelength calibration performed. Time-dependent sensitivity corrections were applied to the COS data, resulting in an absolute flux accuracy of 5%. As the COS data were taken during the LETGS observations, we needed to adjust them to the higher flux levels during the XMM-Newton observations. The OM data at somewhat longer wavelengths (see below)

show on average 6% higher flux during the XMM-Newton observations compared to the LETGS observations. Using the near-simultaneous FUSE/HST/optical spectrum of Mrk 509 from Shang et al. (2005) normalised to the OM flux, we find that increasing the COS flux by 10% is appropriate if assuming a constant shape for the UV spectrum.

6.4. Optical SED

The optical part of the SED was obtained from the OM data. The data were corrected for interstellar absorption and de-reddened using the reddening curve of Cardelli et al. (1989), including the near-UV update by O'Donnell (1994). The total colour excess $E(B - V)$ is 0.057 mag, and $R_V = A(V)/E(B - V)$ was fixed at 3.1. The total neutral hydrogen column density in the direction of Mrk 509 is 4.44×10^{24} m^{-2}, as given by Murphy et al. (1995). The host galaxy correction is based on the results of Bentz et al. (2009) and Kinney et al. (1996). For Mrk 509 the host-galaxy contribution at 2231 Å is 7×10^{-20} W m^{-2} Å^{-1}, which is negligible compared to the AGN flux of 8.45×10^{-17} W m^{-2} Å^{-1}. At longer wavelengths the host galaxy contribution increases, to 3.2×10^{-18} W m^{-2} Å^{-1} at 5500 Å, where the AGN flux is 1.7×10^{-17} W m^{-2} Å^{-1}. For a more thorough description of the optical data reduction, see Mehdipour et al. (2011). The optical fluxes (from Swift UVOT) at the time of the LETGS observations have to be adjusted for the lower flux level of the source. As XMM-Newton observation 2 has a similar flux to that of Swift UVOT observation 18, which is close in time to the LETGS observations, we assume that the optical flux during the LETGS observations is the same as that of XMM-Newton OM observation 2, which is 6% smaller than the average optical flux during the XMM observations.

6.5. Infrared and radio SED

At IR wavelengths shortward of 1 μm, the spectrum shows a small upturn due to emission from the torus (see, e.g., the spectra by Landt et al. 2011). The infrared fluxes that we use here are based on photometry with host-galaxy subtraction in the J, H, and K bands. We use the average from the observations of Danese et al. (1992) and Kotilainen et al. (1992), which are in good agreement with each other. For 100 μm, we use the IRAS flux (Moshir et al. 1990). Between the K-band and the 100 μm flux points, the SED shows an almost constant value in terms of νF_ν. In the 6–35 μm band Spitzer data exist (Wu et al. 2009), with $\sim$ 30% higher flux compared to our adopted SED. However, these data, taken with a relatively large aperture of 10″, are not corrected for the stellar contribution. As our results are not very sensitive to the details of the IR spectrum, we can safely use our simplified SED in the mid-IR band as shown in Fig. 3.

Beyond 100 μm, the flux drops rapidly; following usual practice in this region, we extrapolate the flux from 100 μm to lower frequencies with an energy index of −2.5 down to 1 cm. This gives a flux of only about a factor of two above the observed value at 14.9 GHz (Barvainis et al. 1996). Finally, we also consider an SED without IR emission, because it is unclear how much of the IR emission is seen by the outflow (see next section).

6.6. Effect of the SED on the ionisation balance

Because a different SED can have a strong effect on the ionisation balance of the outflow, we investigated the effects of differ-
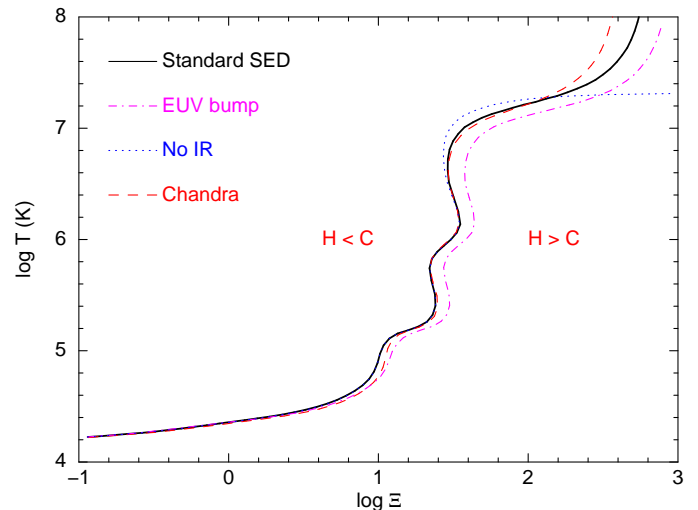

Fig. 4. The four different cooling curves for the different assumed SEDs.

ent SEDs, focusing on the uncertainties in the EUV and infrared parts of the spectrum. In the EUV band we have no measurements, so we have to rely on interpolation. Depending on the location of the outflow relative to the dusty torus expected to surround the AGN, it may receive either all or only a small fraction of the IR flux emitted by the torus. To investigate the effects of different assumptions about this, we compare four SEDs (Fig. 3):

1. Our standard SED (Table 2, column 3 and Fig. 2, solid line), which uses a simple power-law interpolation between the soft X-ray and UV bands;
2. A SED with a stronger EUV flux, using the broken power-law approximation with a break at 193 Å mentioned in Sect. 6.2, to mimic a stronger EUV flux (EUV bump in Fig. 3);
3. Same as model 1, but with the infrared flux essentially set to zero, for an absorber that does not receive emission from the torus (No IR in Fig. 3);
4. the SED for the Chandra observation (Table 2, column 4), to see the effects of time variability.

The ionisation balance calculations were performed using Cloudy[1] (Ferland et al. 1998) version C08.00, with Lodders et al. (2009) abundances. The results are shown in Fig. 4. As can be seen, the differences between the four cooling curves are small. The case without infrared flux (model 3) starts deviating from the default case above 10^6 K, because of enhanced cooling by inverse Compton scattering of the infrared photons. The case with a stronger EUV flux (model 2) has a similar shape to model 1, but has on average $\log \Xi$ higher by 0.08 due to the enhanced ionising EUV flux. This results in a small shift towards the right of the figure. Finally, the lower flux during the Chandra observations leads to a very similar cooling curve, because the peak of the UV spectrum is very similar.

We are therefore confident that our derived SED is an accurate description of the true source continuum of Mrk 509 and that the photo-ionisation results obtained from the analysis of Detmers et al. (2011) are not seriously affected by the uncertainties in the assumed SED.

As an additional test we checked how metallicity influences the cooling curve. We did this because we do not know a priori
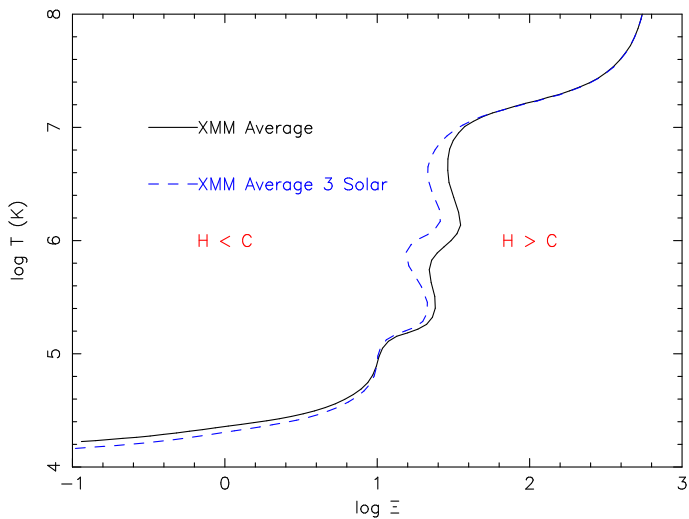
---

[1] http://www.nublado.org/

Fig. 5. The two different cooling curves for solar (solid line) and 3 times solar metallicity (dashed line).

the metallicity of the outflow, which can have a significant effect on the shape of the cooling curve (see e.g. Chakravorty et al. 2009). We adopted 3 times the solar abundances, cf. typical abundances found in Mrk 279 (Arav et al. 2007). Figure 5 shows the results compared to the solar metallicity run. There are slight differences in the shape of the two cooling curves, with the higher metallicity curve having bigger unstable branches (where the slope is negative) due to enhanced line cooling. However, the resulting photo-ionisation model will give no significant differences in derived parameters, except for the hydrogen column densities, which are a factor of three lower owing to the three times higher metal abundances. This again shows that the ionisation structure of the outflow in Mrk 509 is very stable to the uncertainties that are present in either the assumed SED or metallicity.

7. Summary

In this paper we have introduced our multiwavelength study of the Seyfert 1 galaxy Mrk 509, which used XMM-Newton, INTEGRAL, Chandra, HST, Swift, WHT and PAIRITEL. Our observations spanned 100 days of monitoring from September 2009 to December, covering band-passes from 2 μm to 200 keV. The core of our programme consisted of ten simultaneous observations with XMM-Newton and INTEGRAL, followed by a long Chandra LETGS spectrum obtained simultaneously with an HST/COS far-UV spectrum. The high-resolution spectroscopy combined with the time variability monitoring enabled us to disentangle the different absorption and emission components in Mrk 509.

Using our data we produced a continuous light curve in the X-ray and UV bands and a comprehensive SED. Thanks to our broad-band coverage, we deduced that uncertainties on the SED have little effect on the photo-ionisation equilibrium that applies to our subsequent models of the ionised outflow. Our light curve shows a 60% flux increase in the soft X-ray band correlated with an enhancement of the UV flux.

A series of subsequent papers will elaborate on these results and others from our campaign. The stacked XMM-Newton RGS spectrum is presented in Kaastra et al. (2011, paper II). The time-averaged ionisation and velocity structure of the outflow deduced from this spectrum is presented by Detmers et al.

(2011, paper III), the broad-band continuum variability by Mehdipour et al. (2011, paper IV). Ebrero et al. (2011, paper V) describes the Chandra LETGS data and Kriss et al. (2011, paper VI) presents the analysis of the HST/COS data. More papers are in preparation.

References

Allen, D. A. 1976, ApJ, 207, 367
Aoki, K., Oyabu, S., Dunn, J. P., et al. 2011, PASJ, in press (arXiv1101.4340)
Arav, N., , & et al. 2011, ApJ, submitted
Arav, N., Gabel, J. R., Korista, K. T., et al. 2007, ApJ, 658, 829
Baldwin, J., Ferland, G., Korista, K., & Verner, D. 1995, ApJ, 455, L119+
Barvainis, R., Lonsdale, C., & Antonucci, R. 1996, AJ, 111, 1431
Beckmann, V., Shrader, C. R., Gehrels, N., et al. 2005, ApJ, 634, 939
Behar, E., Rasmussen, A. P., Blustin, A. J., et al. 2003, ApJ, 598, 232
Bentz, M. C., Peterson, B. M., Netzer, H., Pogge, R. W., & Vestergaard, M. 2009, ApJ, 697, 160
Bianchi, S., La Franca, F., Matt, G., et al. 2008, MNRAS, 389, L52
Blandford, R. D. & Begelman, M. C. 1999, MNRAS, 303, L1
Blandford, R. D. & Begelman, M. C. 2004, MNRAS, 349, 68
Borgani, S., Governato, F., Wadsley, J., et al. 2002, MNRAS, 336, 409
Bower, R. G., Benson, A. J., Lacey, C. G., et al. 2001, MNRAS, 325, 497
Cappi, M., Tombesi, F., Bianchi, S., et al. 2009, A&A, 504, 401
Cardelli, J. A., Clayton, G. C., & Mathis, J. S. 1989, ApJ, 345, 245
Cavaliere, A., Lapi, A., & Menci, N. 2002, ApJ, 581, L1
Chakravorty, S., Kembhavi, A. K., Elvis, M., & Ferland, G. 2009, MNRAS, 393, 83
Chapman, G. N. F., Geller, M. J., & Huchra, J. P. 1985, ApJ, 297, 151
Ciotti, L. & Ostriker, J. P. 2001, ApJ, 551, 131
Cooke, B. A., Ricketts, M. J., Maccacaro, T., et al. 1978, MNRAS, 182, 489
Costantini, E., Kaastra, J. S., Arav, N., et al. 2007, A&A, 461, 121
Costantini, E., Kaastra, J. S., Korista, K., et al. 2010, A&A, 512, A25
Crenshaw, D. M., Boggess, A., & Wu, C. 1995, AJ, 110, 1026
Crenshaw, D. M., Kraemer, S. B., Boggess, A., et al. 1999, ApJ, 516, 750
Dadina, M. 2008, A&A, 485, 417
Dadina, M., Cappi, M., Malaguti, G., Ponti, G., & de Rosa, A. 2005, A&A, 442, 461
Dahari, O. & De Robertis, M. M. 1988, ApJS, 67, 249
Daly, R. A. & Loeb, A. 1990, ApJ, 364, 451
Danese, L., Zitelli, V., Granato, G. L., et al. 1992, ApJ, 399, 38
de Bruyn, A. G. & Sargent, W. L. W. 1978, AJ, 83, 1257
Detmers, R. G., Kaastra, J. S., Costantini, E., et al. 2010, A&A, 516, A61
Detmers, R. G., Kaastra, J. S., Steenbrugge, K. C., et al. 2011, A&A, in press (paper III)
Dil, S., Primini, F. A., Basinska, E., et al. 1981, ApJ, 250, 513
Dower, R. G., Bradt, H. V., Doxsey, R. E., Johnston, M. D., & Griffiths, R. E. 1980, ApJ, 235, 355

Dunn, J. P., Bautista, M., Arav, N., et al. 2010, ApJ, 709, 611
Ebrero, J., Kriss, G. A., Kaastra, J. S., et al. 2011, A&A, in press (paper V)
Ferland, G. J., Korista, K. T., Verner, D. A., et al. 1998, PASP, 110, 761
Fuentes-Williams, T. & Stocke, J. T. 1988, AJ, 96, 1235
Furlanetto, S. R. & Loeb, A. 2001, ApJ, 556, 619
Gabel, J. R., Kraemer, S. B., Crenshaw, D. M., et al. 2005, ApJ, 631, 741
Glass, I. S. 2004, MNRAS, 350, 1049
Glass, I. S., Moorwood, A. F. M., & Eichendorf, W. 1982, A&A, 107, 276
Haardt, F. 1993, ApJ, 413, 680
Haardt, F. & Maraschi, L. 1991, ApJ, 380, L51
Haardt, F., Maraschi, L., & Ghisellini, G. 1997, ApJ, 476, 620
Hamann, F. W., Barlow, T. A., Chaffee, F. C., Foltz, C. B., & Weymann, R. J. 2001, ApJ, 550, 142
Huchra, J., Latham, D. W., da Costa, L. N., Pellegrini, P. S., & Willmer, C. N. A. 1993, AJ, 105, 1637
Jourdain, E., Bassani, L., Bouchet, L., et al. 1992, A&A, 256, L38
Kaastra, J. S., De Vries, C. P., Steenbrugge, K. C., et al. 2011, A&A, submitted (paper II)
Kaastra, J. S., Raassen, A. J. J., Mewe, R., et al. 2004, A&A, 428, 57
Kaastra, J. S., Steenbrugge, K. C., Raassen, A. J. J., et al. 2002, A&A, 386, 427
King, A. 2003, ApJ, 596, L27
Kinney, A. L., Calzetti, D., Bohlin, R. C., et al. 1996, ApJ, 467, 38
Kirhakos, S. D. & Steiner, J. E. 1990, AJ, 99, 1435
Kopylov, I. M., Lipovetskii, V. A., Pronik, V. I., & Chuvaev, K. K. 1974, Astrofizika, 10, 483
Kotilainen, J. K., Ward, M. J., Boisson, C., Depoy, D. L., & Smith, M. G. 1992, MNRAS, 256, 149
Kraemer, S. B., Crenshaw, D. M., Gabel, J. R., et al. 2006, ApJS, 167, 161
Kraemer, S. B., Crenshaw, D. M., Yaqoob, T., et al. 2003, ApJ, 582, 125
Kriss, G. A., Arav, N., Kaastra, J. S., et al. 2011, A&A, in press (paper VI)
Kriss, G. A., Green, R. F., Brotherton, M., et al. 2000, ApJ, 538, L17
Kronberg, P. P., Dufton, Q. W., Li, H., & Colgate, S. A. 2001, ApJ, 560, 178
Krongold, Y., Nicastro, F., Brickhouse, N. S., et al. 2003, ApJ, 597, 832
Krongold, Y., Nicastro, F., Elvis, M., et al. 2007, ApJ, 659, 1022
Landt, H., Elvis, M., Ward, M. J., et al. 2011, MNRAS, in press (ArXiv1101.3342)
Liu, R. 1983, Acta Astrophysica Sinica, 3, 113
Lodders, K., Palme, H., & Gail, H. 2009, in Landolt-Börnstein - Group VI Astronomy and Astrophysics Numerical Data and Functional Relationships in Science and Technology Volume 4B: Solar System. Edited by J.E. Trümper, 2009, 4.4., 44
Longinotti, A. L., Costantini, E., Petrucci, P. O., et al. 2010, A&A, 510, A92
MacKenty, J. W. 1990, ApJS, 72, 231
Magnitskaia, O. V. & Saakian, K. A. 1976, Astrofizika, 12, 431
Maisack, M., Johnson, W. N., Kinzer, R. L., et al. 1993, ApJ, 407, L61
Malzac, J. & Jourdain, E. 2000, A&A, 359, 843
Markarian, B. E. 1973, Astrofizika, 9, 5
Markarian, B. E. & Lipovetskij, V. A. 1973, Astrofizika, 9, 487
Martin, P. G., Thompson, I. B., Maza, J., & Angel, J. R. P. 1983, ApJ, 266, 470
McAlary, C. W., McLaren, R. A., McGonegal, R. J., & Maza, J. 1983, ApJS, 52, 341
Mediavilla, E., Arribas, S., Garcia-Lorenzo, B., & del Burgo, C. 1998, ApJ, 494, L9
Mehdipour, M., Branduardi-Raymont, G., Kaastra, J. S., et al. 2011, A&A, in press (paper IV)
Mingaliev, M. G., Pustilnik, S. A., Trushkin, S. A., Kirakosian, R. M., & Malumian, V. G. 1978, Astrofizika, 14, 91
Moe, M., Arav, N., Bautista, M. A., & Korista, K. T. 2009, ApJ, 706, 525
Moorwood, A. F. M. 1986, A&A, 166, 4
Morini, M., Lipani, N. A., & Molteni, D. 1987, ApJ, 317, 145
Moshir, M., Kopan, G., Conrow, T., et al. 1990, in IRAS Faint Source Catalogue, version 2.0 (1990)
Murphy, E. M., Lockman, F. J., & Savage, B. D. 1995, ApJ, 447, 642
Mushotzky, R. F., Marshall, F. E., Boldt, E. A., Holt, S. S., & Serlemitsos, P. J. 1980, ApJ, 235, 377
Nandra, K., Le, T., George, I. M., et al. 2000, ApJ, 544, 734
Netzer, H., Kaspi, S., Behar, E., et al. 2003, ApJ, 599, 933
O'Donnell, J. E. 1994, ApJ, 422, 158
Ogle, P. M., Mason, K. O., Page, M. J., et al. 2004, ApJ, 606, 151
Osterbrock, D. E. 1977, ApJ, 215, 733
Page, M. J., Davis, S. W., & Salvi, N. J. 2003, MNRAS, 343, 1241
Perola, G. C., Matt, G., Cappi, M., et al. 2002, A&A, 389, 802
Peterson, B. M., Crenshaw, D. M., Meyers, K. A., Byard, P. L., & Foltz, C. B. 1984, ApJ, 279, 529
Peterson, B. M., Ferrarese, L., Gilbert, K. M., et al. 2004, ApJ, 613, 682
Peterson, B. M., Foltz, C. B., Byard, P. L., & Wagner, R. M. 1982, ApJS, 49, 469
Peterson, B. M., Wanders, I., Bertram, R., et al. 1998, ApJ, 501, 82
Petrucci, P. O., Haardt, F., Maraschi, L., et al. 2001, ApJ, 556, 716

Petrucci, P. O., Haardt, F., Maraschi, L., et al. 2000, ApJ, 540, 131
Petrucci, P. O., Maraschi, L., Haardt, F., & Nandra, K. 2004, A&A, 413, 477
Petrucci, P.-O. et al. 2011, A&A, in preparation
Phillips, M. M., Baldwin, J. A., Atwood, B., & Carswell, R. F. 1983, ApJ, 274, 558
Pietsch, W., Reppin, C., Truemper, J., et al. 1981, A&A, 94, 234
Platania, P., Burigana, C., De Zotti, G., Lazzaro, E., & Bersanelli, M. 2002, MNRAS, 337, 242
Ponti, G., Cappi, M., Vignali, C., et al. 2009, MNRAS, 394, 1487
Pounds, K., Reeves, J., O'Brien, P., et al. 2001, ApJ, 559, 181
Pounds, K. A., Nandra, K., Fink, H. H., & Makino, F. 1994, MNRAS, 267, 193
Poutanen, J. & Svensson, R. 1996, ApJ, 470, 249
Reeves, J. N., Nandra, K., George, I. M., et al. 2004, ApJ, 602, 648
Rieke, G. H. 1978, ApJ, 226, 550
Roche, P. F., Whitmore, B., Aitken, D. K., & Phillips, M. M. 1984, MNRAS, 207, 35
Rosenblatt, E. I., Malkan, M. A., Sargent, W. L. W., & Readhead, A. C. S. 1992, ApJS, 81, 59
Rothschild, R. E., Baity, W. A., Gruber, D. E., et al. 1983, ApJ, 269, 423
Scannapieco, E. & Oh, S. P. 2004, ApJ, 608, 62
Shang, Z., Brotherton, M. S., Green, R. F., et al. 2005, ApJ, 619, 41
Silk, J. & Rees, M. J. 1998, A&A, 331, L1
Singh, K. P., Garmire, G. P., & Nousek, J. 1985, ApJ, 297, 633
Singh, K. P. & Westergaard, N. J. 1992, A&A, 264, 489
Smith, R. A. N., Page, M. J., & Branduardi-Raymont, G. 2007, A&A, 461, 135
Steenbrugge, K. C., Fenovčík, M., Kaastra, J. S., Costantini, E., & Verbunt, F. 2009, A&A, 496, 107
Steenbrugge, K. C., Kaastra, J. S., Crenshaw, D. M., et al. 2005, A&A, 434, 569
Steenbrugge, K. C., Kaastra, J. S., de Vries, C. P., & Edelson, R. 2003, A&A, 402, 477
Stein, W. A. & Weedman, D. W. 1976, ApJ, 205, 44
Stern, B. E., Poutanen, J., Svensson, R., Sikora, M., & Begelman, M. C. 1995, ApJ, 449, L13
Svensson, R. 1996, A&AS, 120, C475
Ulvestad, J. S. & Wilson, A. S. 1984, ApJ, 278, 544
Unger, S. W., Lawrence, A., Wilson, A. S., Elvis, M., & Wright, A. E. 1987, MNRAS, 228, 521
Winge, C., Storchi-Bergmann, T., Ward, M. J., & Wilson, A. S. 2000, MNRAS, 316, 1
Wu, C., Boggess, A., & Gull, T. R. 1980, ApJ, 242, 14
Wu, K. K. S., Fabian, A. C., & Nulsen, P. E. J. 2000, MNRAS, 318, 889
Wu, Y., Charmandaris, V., Huang, J., Spinoglio, L., & Tommasin, S. 2009, ApJ, 701, 658
Wyithe, J. S. B. & Loeb, A. 2003, ApJ, 595, 614
Zdziarski, A. A., Ghisellini, G., George, I. M., et al. 1990, ApJ, 363, L1
Zdziarski, A. A. & Grandi, P. 2001, ApJ, 551, 186